P 2mif

NASA TECHNICAL MEMORANDUM

NASA TM X-71559

NASA TM X-71559

HOT ION PLASMA HEATING EXPERIMENTS IN SUMMA

by J. J. Reinmann, M. R. Lauver, R. W. Patch,
S. J. Posta, A. Snyder, and G. W. Englert
Lewis Research Center
Cleveland, Ohio 44135

TECHNICAL PAPER proposed for presentation at
First International Conference on Plasma Science
sponsored by the Institute of Electrical
and Electronics Engineers
Knoxville, Tennessee, May 15-17, 1974

HOT ION PLASMA HEATING EXPERIMENTS IN SUMMA

J. J. Reinmann, M. R. Lauver,
R. W. Patch, S. J. Posta,
A. Snyder, and G. W. Englert

NASA Lewis Research Center
Cleveland, Ohio 44135

SUMMARY AND ABSTRACT

Initial results are presented for the hot-ion plasma heating experiments conducted in the new SUMMA (Superconducting Magnetic Mirror Apparatus) at NASA Lewis Research Center. A discharge is formed by applying a radially inward dc electric field between cylindrical anodes and hollow cathodes located at the peak of the mirrors. Data were obtained at midplane magnetic field strengths from 1.0 to 3.5 tesla. Charge-exchange neutral particle energy analyzer data were reduced to ion temperatures using a plasma model that included a Maxwellian energy distribution superimposed on an azimuthal drift, finite ion orbits, and radial variations in density and electric field. The best ion temperatures in a helium plasma were 5 keV and in hydrogen the H_2^+ and H^+ ions were 1.2 keV and 1 keV respectively. Optical spectroscopy line broadening measurements yielded ion temperatures about 50 percent higher than the charge-exchange neutral particle analyzer results. Spectroscopically obtained electron temperatures ranged from 3 to 30 eV. Ion temperature was found to scale roughly linearly with the ratio of power input-to-magnetic field strength, P/B. Thus, to achieve high ion temperatures at high magnetic field will require increased electrode voltage and currents. Operation at higher magnetic fields is desired because theory indicates that the charged particle density may scale as the square of magnetic field strength.

INTRODUCTION

This report presents the initial results of the hot ion plasma heating experiments conducted in the new superconducting magnetic mirror facility (SUMMA) at the NASA Lewis Research Center (ref. 1). This research is a continuation of the hot ion plasma (HIP-1) program at LeRC (ref. 2, 3, 4). The purpose of these experiments was twofold: (1) to make a reliable electrode assembly for steady-state operation in the new SUMMA magnetic field configuration and test-section geometry; and (2) to see how ion heating scales as the midplane magnetic field is varied up to 3.5 tesla. In HIP-1 the maximum midplane field was 1.5 tesla, and

in similar plasma heating experiments at Oak Ridge National Laboratory (ref. 5) the maximum midplane field was 2.5 tesla. Results are reported for helium and hydrogen plasmas.

In this heating scheme energy is coupled to the plasma by applying a radially inward dc electric field near the maximum field region of a magnetic mirror. Under the influence of the mutually perpendicular electric, E, and magnetic, B, fields the ions drift azimuthally with a velocity near E/B. The energy corresponding to this drift, $1/2\ m\ E^2/B^2$, can be several kilovolts. It has been predicted theoretically (ref. 6) and observed experimentally (ref. 5) that high frequency (on the order of the ion plasma frequency) electrostatic drift waves are present in this type of plasma configuration. It is possible that the electric fields of these waves heat the plasma ions to energies greater than the drift energy.

The principal diagnostics used were: (1) a charge-exchange neutral-particle energy analyzer (NPA) to obtain the energy spectra of individual plasma ion species; and (2) an optical spectrometer to estimate ion temperatures via doppler line broadening and electron temperature via line intensity ratio techniques. Measurements were made for the plasma impurities as well as the primary species. The NPA electronics that were developed to obtain rapid sweeps of the energy distribution of a single ion species are also described herein. Ion temperatures were obtained from the NPA data using a plasma model that included an azimuthal drift velocity superimposed upon a Maxwellian energy distribution, finite ion gyro radii, and radial variations in both ion density and electric field. The details of this plasma model are presented in a companion paper to be presented in this symposium (ref. 7).

APPARATUS

A superconducting magnetic mirror apparatus (SUMMA) was constructed at NASA Lewis Research Center for use in thermonuclear research (ref. 1; see figure 1). The SUMMA facility is unique in that it has the highest design field strengths for its bore size of any known facility employing superconducting magnets.

Magnet Facility

The SUMMA facility includes four solenoidal magnets and three spacers permitting several different magnetic field configurations. Each magnet has an inner, middle, and outer winding that can be individually powered for further flexibility in shaping the magnetic field. The magnet bore is open to atmosphere, and each spacer has horizontal and vertical ports open to atmosphere thereby providing radial access to the magnet bore. The experimental volume of the magnet bore is therefore completely isolated from the magnet facility vacuum. The plasma test section can be

opened up and modifications to the experiments can be made while the magnets remain at liquid helium temperatures. The design parameters and construction details of the superconducting magnets are already in the literature (ref. 8, 9). The major parameters of SUMMA for the simple mirror configuration are listed in Table I. A cutaway view of the facility is shown in figure 2.

In the tests reported herein, only the two inboard magnets were powered because one of the outboard magnets was being rewound. This fourth magnet has now been tested and will be installed.

Plasma Test Section

A schematic view of the plasma test section and magnet configuration is shown in figure 3. The two outboard magnets are drawn with dashed lines since they were not used for the tests reported herein. The discharge chamber is a cylinder 3.75 m in length and 36.6 cm in diameter made from 304 stainless steel. A ten-inch diffusion pump at each end of the test section pumps the system down to about 5×10^{-7} torr. The center ports are located both vertically and horizontally. They are used for visual observation, charge-exchange neutral particle diagnostics, and optical spectroscopy. Two 25 cm diameter ports at the ends of the test section provide excellent viewing of the plasma via the mirrors shown.

The centerline magnetic field profile is also shown in figure 3. The maximum midplane magnetic field was 3.5 tesla.

Electrode Assembly

Also shown schematically in figure 3 are the anodes, cathodes, and electrically-floating plates. Figure 4 is a photograph of the electrode assembly removed from the test section. Discoloration on the white aluminum oxide insulators is sputtered metal that is normally found after prolonged operation of the discharge.

A cathode cross section is shown in figure 5. Gas in introduced through the cathodes to produce a hollow-cathode discharge. The tungsten cathodes are uncooled, and therefore the energy they receive by hot-ion and charge-exchange neutral bombardment must be radiated away. The cathodes are located on axis with their tips placed at the peaks of the mirrors. The water-cooled anode rings are toroids with a 3.3 cm major diameter and a 9.5 mm minor diameter, and are made from 304 stainless steel tubing of 0.8 mm wall thickness. The anodes are electrically grounded to the test-section walls. In reference 2 it was determined that the optimum position of the anode was 7.5 cm in front of the cathode tips.

The electrically-floating shield shown in figures 3 and 4 protects the cathode holder from charge-exchange neutral and ion bombardment and helps inhibit arcing along the magnetic field lines from the cathode holder to the grounded anode rings. These plates were uncooled for the results reported herein.

The electrodes are connected to a 0-20 kV, 0-10 amp power supply. To insure stable operating characteristics a 2000 ohm ballast resistor is used in series with the output of the power supply. The current is divided between the two cathodes, and their currents are individually measured. Supply currents range typically from 0.2 amp to about 1.5 amp. The electrode voltage is limited to 20 kV minus the voltage drop across the ballast resistor. Presently, total input power is limited by overheating of the floating shields.

Gas flow to each cathode is remotely controlled by a precision variable-leak. Gas flows are adjusted to maintain approximately equal current on each cathode.

Charge-Exchange Neutral Particle Analyzer

A schematic of the charge-exchange neutral particle analyzer (NPA) is shown in figure 6. The energy analyzer section of the NPA is a duplicate of the one described in reference 10. Those charge-exchanged neutrals which enter the aperture of the collimator are reionized in a gas stripping cell. The charged particles emerging from the gas cell are then separated according to energy by passing through the 90° electrostatic deflection plates. When the detector is placed at position 1 immediately behind the output slit of the deflector plates, the detector current as a function of energy $I(E)$ is obtained by sweeping the voltage on the plates. A complete sweep takes a second or so. These spectra do not distinguish particles according to mass, only energy. When the detector at position 1 is moved out of the path of the ions, the ions of a given energy pass into a 90° bending magnet, and the various mass species are separated out. Thus for a given voltage on the electrostatic deflection plates there exists a magnetic field for which only ions of a given energy and mass can pass through the slit and be detected. Use of the complete analyzer allows one to determine particle current as a function of energy for each mass separately.

The NPA sampled from a chord of plasma approximately 0.5 cm high (vertical) and 1 cm wide (parallel to the magnetic field). The NPA apparatus was mounted so that the plasmas could be scanned vertically by pivoting the beam line about a point so designated on figure 6.

To obtain the energy distribution within the plasma from the energy distribution $I(E)$ at the detector output requires a model of the plasma and a knowledge of the energy dependence of those factors that relate the

detector current to the charge-exchange neutral current. These factors include the charge-exchange between plasma ions and the neutral background gas, the nitrogen gas stripping cell conversion efficiency, particle detector secondary emission coefficient, and also the effects of plasma rotation, density gradients, and large ion gyroradii. We have attempted to take all of these factors into account in a companion paper presented at this meeting (ref. 7). In the present report the NPA data were reduced to ion temperatures in accordance with the theoretical model given in reference 7. Details of the NPA detector and electronics system are provided in Appendix A.

Apparatus for Emission Spectroscopy

The apparatus for emission spectroscopy is shown in figure 7. It was located at the midplane of the magnetic mirror and viewed the plasma perpendicular to the magnetic axis. The vertical centerplane was focused on the entrance slit of a spectrometer by means of a lens. Between the lens and the entrance slit the beam was rotated 90° by means of a beam rotator consisting of totally reflecting prisms and mirrors. A stop was provided to reduce the vertical height of the beam. With this arrangement the area of the vertical centerplane viewed by the spectrometer was determined by the size and shape of the entrance slit and was approximately 2 mm high by 26 mm long. Since most of the light from the plasma came from inside a 54 mm plasma diameter, the vertical resolution of the optics was about 4 mm after allowance for beam divergence. This resolution is superior to that previously achieved in HIP with a two-slit collimator (ref. 2).

Vertical scanning of the plasma was accomplished by means of a table with pivot and adjustable screw (fig. 7). The spectrometer, beam rotator, stop, and lens were rigidly secured to the table. Hence chords of the plasma above and below the horizontal centerplane of the apparatus could be viewed. The vertical distance of the chord from the plasma centerline is designated y (fig. 7).

The grating spectrometer employed an f/8.6 $\frac{1}{2}$ m Ebert mounting with curved slits. The reciprocal linear dispersion was 1.6 nm/mm in first order. Detection was by means of film or a magnetically shielded photomultiplier with S13 photocathode.

DISCUSSION OF RESULTS

In this section we discuss the NPA data and the optical spectrometer data. There is also a discussion of our visual observations since this was an essential diagnostic in guiding our electrode design modifications and in the interpretation of NPA results.

Neutral Particle Analyzer Results

Effect of electrode voltage:- Figure 8 shows the raw NPA energy distribution data for helium at several electrode voltages with the magnetic field and electrode current held fixed. Figure 8 illustrates the excellent signal-to-noise ratio that can be achieved with the NPA apparatus. Table II lists the discharge conditions for each of the curves on figure 8. In figure 8, we see that both the most probable energy, $\mathcal{E}_p$, and the half width, $\Delta\mathcal{E}$, increase as the electrode voltage is raised. According to Table II the detector signal at $\mathcal{E}_p$, and therefore area under the curves, increases with increasing electrode voltage. Thus, both ion temperature and the number of particles reaching the detector increase with increasing power. Since the neutral background pressure was reduced as the electrode voltage was raised (see Table II) the increased area under the curves suggests that the ion density increases with power. Therefore, increased power goes into both ion heating and ion production, making this an attractive ion heating device.

Another aspect of figure 8 is the actual shapes of the curves which are not typical of a simple Maxwellian energy distribution. The flat, low-signal portion of the curves at the low energies suggests a drift motion superimposed on a randomized energy distribution. This is borne out by the plasma model used to reduce the data (ref. 7) where a drift motion had to be included to obtain a good fit to the data. Figure 9 shows how well the plasma model can fit the NPA data. Table III lists the plasma discharge conditions, the ion temperature, T_i, electric field, E, and ExB drift energy which were computed from the plasma model. The computed drift energy decreased while the ion energy increased with increasing electrode voltage. This would suggest that the plasma is heated by other means as well as the drift energy.

Effect of electrode current:- Figure 10 shows the effect of electrode current (total power supply current) on the NPA energy spectrums for hydrogen H^+ ions. Table IV lists the plasma discharge conditions for the curves of figure 10, and indicates that the electrode voltage and magnetic field were held constant. While $\mathcal{E}_p$ is almost constant, the curves broaden and the area under the curves increases with current and consequently with power. These results agains suggest that increased power is effective in increasing both the ion temperature and the number of ions in the plasma. While the curves of figures 8-10 might suggest that $\mathcal{E}_p$ is controlled by the electrode voltage, other data under different plasma conditions show that $\mathcal{E}_p$ can also be shifted by varying the current.

Relative detector signals for H^+, H_2^+, and C^+ in a hydrogen plasma:- Figure 11 shows the relative amplitudes of the NPA detector signal for H^+, H_2^+, and C^+ for a given plasma condition. Both H^+ and H_2^+ are about equal in magnitude, while C^+ is approximately 1/3 the amplitude of the others. We do not know the energy dependence for each process that the

carbon ion must undergo in its path from the plasma to the NPA detector. But this is a relatively strong signal. The carbon is probably coming from the stainless steel anodes and test section wall, with perhaps some coming from the vacuum pump oils. In contrast to these results, after several months of operation in HIP-1, the carbon signal was observed to be less than ten percent of the helium signal. We attributed the lower carbon signal in HIP-1 to cleaning or depletion of carbon on the stainless steel components via ion and charge-exchange neutral bombardment. As noted earlier, the SUMMA test section pumps down to about 5×10^{-7} torr when the gas feed is shut off. Thus, in spite of the relatively short operating time in SUMMA, the test section is fairly clean.

In spite of the strong carbon signals measured with the NPA, we were not able to observe carbon lines in the visible spectrum with optical spectroscopy. This is discussed further in the section on optical spectroscopy. Other heavy masses with mass-to-charge ratios 6, 12, 13, 14, 15, 16, 17, 18, 24, 28, 32, 35, 40, 44, and 56 were observed with the NPA and with the exception of N^+ and O^+ their signal strengths were very low.

Our results show that if a momentum analyzer is not used, and only a composite energy spectrum for all masses is measured, the tail of the distribution could be dominated by the impurity ions and the molecular plasma species. Thus the temperature inferred from such data may be that of the molecular plasma species and the impurities rather than the desired atomic species. Some independent check is needed to rule out this possibility especially in a high energy, high density plasma where severe wall and electrode bombardment are likely.

Effect of magnetic field on ion temperature:- Figure 12 is a plot of helium ion temperature against electrode voltage with midplane magnetic field as a parameter. The plasma conditions for these data are listed in Table V. We see that the ion temperature increases with electrode voltage. The slope of the curves at a given electrode voltage, V, is almost inversely proportional to the magnetic field strength which again suggests that the driving energy is a strong function of V/B. In figure 12 the electrode current was decreased with increasing magnetic field. Power input is limited by plasma heating of the uncooled floating shields (see fig. 3 and 4). At the highest magnetic fields the electrode currents are limited to relatively low values to avoid overheating of the floating plates. We visually observed that as the magnetic field strength was increased the plasma column became more radially constricted, and the floating shields rapidly heated to yellow or white hot in a thin region around the hole. This heating of the shield was accompanied by rapid current increases such that steady state discharge conditions could not be maintained. It is possible that the shield provides a low resistance path across magnetic field lines when it becomes an electron emitter at the higher temperatures. The path envisioned is from the cathode tip along a magnetic field line to the shields, through the shield across

magnetic field lines, and from the shield along a field line to the anode. The constriction of the plasma column at the higher magnetic fields may be due to better radial plasma containment.

According to one theory (ref. 5) for this heating scheme, the density should scale as the square of the magnetic field. Thus, to achieve higher densities, we want to operate at the highest magnetic field strengths. The curves of figure 12 and our visual observations make it quite clear what must be done to obtain higher densities and higher ion temperatures. We must operate at higher electrode voltages and currents. Higher power operation will require improved electrode cooling. Our present electrode design operates up to 20 kV without either internal or external voltage breakdown. However, we anticipate that for higher voltage and power operation, additional problems will have to be solved.

In general it was easier to control both the electrode current and voltage independently in the helium plasma than in the hydrogen plasma. The specific reason for this is not well understood, but we suspect that electrode surface effects (mainly heating of the surfaces to emitting temperatures) played a strong role. The result is that it was not always possible to obtain a consistent set of data in hydrogen.

For hydrogen, in general, the ion temperature increased with electrode voltage for a fixed electrode current and magnetic field. And the ion temperature decreased at a given electrode voltage and current as the magnetic field strength increased. The molecular ion, H_2^+, temperature was always higher than the atomic ion, H^+, temperature for a given plasma condition, and $\mathcal{E}_p$ for H_2^+ was about twice that for H^+. However, there was more scatter in the results when the simple correlation for helium (fig. 12) was attempted for hydrogen. In addition to the more difficult operation with hydrogen, the calculation of the ion temperature is also more complex. In helium, charge exchange occurs only with the neutral helium atom background. For hydrogen, the ions can charge exchange on three different groups of background neutrals. These consist of molecules, atoms formed by dissociation on hot electrode surfaces, and Franck-Condon neutrals (ref. 12) formed by electron impact dissociation. In calculating the ion temperatures from the detector current energy distributions for hydrogen, we assumed the ions charge exchanged on cold molecular neutrals only.

Figures 13 and 14 show results for hydrogen where it was possible to obtain H^+ and H_2^+ ion temperatures respectively as a function of electrode voltage for constant values of magnetic field and current. As with the helium results, ion temperature increases with electrode voltage for a fixed magnetic field, and at a fixed electrode voltage the temperature decreases with magnetic field strength.

Dependence of ion temperature on power and magnetic fields:- When the ion temperature is plotted against the ratio of power input-to-magnetic field strength for all the data of a given ion species a trend is made apparent. These plots are shown in figures 15, 16, and 17 for He^+, H^+, and H_2^+, respectively. These results again illustrate the need for much higher voltage and current levels to achieve high ion temperatures at the higher magnetic fields. These results are in qualitative agreement with those obtained by optical line broadening measurements as will be discussed in a later section.

Effect of Ion Mass on Temperature:- Figures 12 through 17 show that ion heating is strongly dependent upon the ion mass. Atomic hydrogen is heated the least and helium the most. For a given hydrogen plasma run, $\mathcal{E}_p$ for H_2^+ was always about twice that for H^+. When it was possible to find a helium run with current, voltage, and magnetic field close to a hydrogen run, it was found that the $\mathcal{E}_p$ for He^+ was about twice that for the H_2^+ (see figure 18). If $\mathcal{E}_p$ is associated with the driving energy of the dominant heating mechanism, then that heating mechanism would be proportional to the mass. Such a possible driving energy would be the drift energy, $\frac{1}{2}$ m $(E/B)^2$.

A cross-plot of the curves for 2.7 T on figures 12 to 14 showed that the ion temperature increases about exponentially with mass.

Comparing the trend in figure 15 for helium against that for hydrogen in figures 16 and 17, we see that the helium ion temperature is proportional to P/B raised to about the power of two, while for hydrogen the relation is more nearly linear.

Optical Spectroscopy

The emission spectra of helium and hydrogen were observed in the wavelength range 398 to 672 nm using photoelectric and photographic detection. The three categories of observations were general surveys, line profiles, and line intensity ratios.

General surveys:- General surveys of helium and hydrogen at low magnetic fields and low electrode voltages indicated moderate degrees of ionization and some contamination. Fifteen He, one He^+, and 16 Fe lines were identified in helium at 7.5 kV electrode voltage, 0.61 A total anode-cathode current, 1.38×10^{-4} torr pressure, and 1.39 T magnetic flux density. Four H lines, 119 H_2 lines, and one Ta line were identified in hydrogen at 8.7 to 16.4 kV, 0.42 to 0.54 A, 5.2×10^{-5} to 7.2×10^{-5} torr, and 1.36 to 2.72 T. Failure to observe C lines or molecular bands is not considered conclusive because most strong C lines are outside the wave-

length range observed. In a similar device (ref. 12) no C or C^+ optical spectra were detected even after methane was added to the deuterium, although an NPA detected increased C and H.

Ion temperatures and drift measurements from line profiles:- Observations of line profiles were principally of the He^+ 468.6 nm and H_β 486.1 nm lines. Typical traces are shown in figures 19 to 23. In all cases shown there is an intense, narrow component superimposed on a less intense, wide component. The principal cause of broadening is the Doppler effect, although there is some magnetic splitting and some broadening due to the slit function of the spectrometer. The causes of the two components differ. For helium the narrow component is due to electron impact excitation of He^{+*} from He directly (an asterisk indicates electronic excitation), followed by radiation, whereas the wide component is due to electron impact excitation of He^{+*} from He^+ followed by radiation. For hydrogen the narrow component is attributed to Franck-Condon neutrals (ref. 13) whereas the wide component is due to charge-exchange neutral atoms. For both helium and hydrogen the width of the wide component gives a direct measure of the atomic ion temperature, and the wavelength shift of the wide component relative to the narrow component should indicate the component of ion drift velocity parallel to the line of sight.

Analysis of the traces to determine ion temperature and shift required a four-step procedure. First, the profile of the wide component was determined by fairing out the narrow component and any extraneous lines with a French or ship's curve. Second, the shift was determined by finding the centroid of the area of the wide component. Third, $\overline{(\Delta\lambda)^2}$, the average of the square of the wavelength deviation of the wide component from its centroid was measured. Steps two and three were done with a chart digitizer. Fourth, the temperature, T, was defined by setting

$$\frac{m\overline{v_x^2}}{2} = \frac{1}{2} kT \qquad (1)$$

where m is the mass of the atomic ion or atom, k is Boltzmann's constant, v_x is the random component of velocity along the line of sight relative to the drift, and the bar indicates the average of v_x^2. This definition was used because v_y and v_z could not be observed and is consistent with the usual definition (ref. 14) if $v_x^2 = v_y^2 = v_z^2$. Using Doppler's relation, eq. (1) becomes approximately

$$T = \frac{mc^2}{k\lambda_o^2} \overline{(\Delta\lambda)^2} \qquad (2)$$

where c is the velocity of light and λ_o is the wavelength of the line center.

In the four-step procedure two corrections were omitted. No correction was made for the spectrometer slit function because preliminary work proved that the correction was negligible. No correction was made for magnetic splitting despite Sato, deKock, and Winkel's note (ref. 15) because at the higher magnetic fields the splitting is not described by the Zeeman effect and an adequate treatment was lacking. (The Paschen-Back effect sets in for H at several tenths of a tesla (ref. 16), and this effect was observed for the He 471.3 nm line in SUMMA at 3.52 T.)

Ion temperatures for He^+ are given in figure 24 and Table VI based on eq. (2). In figure 24 the ion temperature is plotted versus the ratio of power input, P, to midplane magnetic flux density, B, for y between -1.35 and +1.35 cm. The ion temperature increases as P/B is increased. In Table VI ion temperatures and conditions are given for $y = 0$. For magnetic flux density from 1.07 to 3.52 T the ion temperature tended to decrease as the flux density increased.

Charge-exchange neutral temperatures for H are given in figure 25 and Table VII. In figure 25 the charge-exchange neutral temperature is plotted versus the ratio of power input to midplane magnetic flux density for y between -2.69 and +2.69 cm. The charge-exchange neutral temperature increased as P/B increased. In Table VII charge-exchange neutral temperatures and discharge conditions are given for $y = 0$. For magnetic fields from 1.07 to 2.72 T the charge-exchange neutral temperature tended to decrease as the magnetic field increased.

The ion temperatures for helium and the charge-exchange neutral temperatures for hydrogen obtained from spectral line profiles tend to be higher than those obtained with the NPA. An appreciable part of these discrepancies is due to the omission of corrections for magnetic splitting in He^+ and H line profiles. Also, both normal and anomalous profiles were observed for the He^+ 468.6 nm line and are shown in figures 19 and 20, respectively. The anomalous profiles could have contributed to the discrepancy in He^+ temperatures. No such anomalies were observed for H_β. However, some interference from H_2 lines was encountered as shown in figures 22 and 23. The vertical gain on the two traces in each figure differed by a factor of ten (in this and following figures with multiple traces, instrument limitations caused the wavelengths of the two traces to be offset slightly relative to each other). It is doubtful if the H_2 interference caused appreciable error in charge-exchange neutral temperatures.

For helium the shift of the wide component relative to the narrow component as the plasma is traversed vertically (see fig. 7 for definition of y) is shown in figure 21. Unfortunately, the shift direction was not always fully reproducible as the plasma was traversed, as figure 26

shows. In any case, the trend is consistent with a Doppler shift caused by a drift velocity. The line-of-sight component of drift energy calculated from the Doppler shift was between 1.8 and 433 eV for all points in figure 26. Shifts for $y = 0$ are given in Table VI and were always positive although they would be expected to be zero. This could be due to any number of causes including the anomalous line profile and possible shift of the narrow component.

For hydrogen the shift of the wide component of H relative to the narrow component as the plasma was traversed vertically is shown in figure 27 for y between -2.69 and +2.69 cm. Again the trend is consistent with a Doppler shift caused by a drift velocity. The line-of-sight component of drift energy calculated from the Doppler shift was between 0 and 34.1 eV for figure 27. Shifts for $y = 0$ are given in Table VII and, just as for He^+, were always positive.

Line intensity ratios:- Observations of line intensity ratios were used to calculate the free electron temperature in helium based on an optically thin corona model (ref. 17-19). Two line ratios were used: (1) ratio of intensities of the He 504.7 nm and He 471.3 nm lines and (2) ratio of intensities of the He 443.8 nm and He 412.1 nm lines. Most observations were made with $y = 0$, but one set was made with various y values and then Abel inverted.

The He line emission was recorded just as for ion temperatures by taking photoelectric traces of emission vs wavelength over the entire width of each line. However, the lines were at appreciably different wavelengths, so a relative intensity calibration of the optical system and detector was necessary. This was accomplished in the usual way with a tungsten strip lamp and two optical pyrometers to measure the brightness temperature of the lamp. The spectral emissivity of tungsten was obtained from reference 20.

To reduce the data from the $y = 0$ runs, the areas of the profiles were measured and ratioed and corrected by means of the relative intensity calibration to yield true intensity ratios. The intensity ratios were converted to free electron temperature by using the cross sections of Latimer, Mills, and Day (ref. 19). Because the intensities included contributions from all plasma radii, the resulting electron temperatures were averages. For each set of conditions, the electron temperature was measured three times using the ratio of intensities of the 504.7 and 471.3 nm lines and three times using the ratio of intensities of the 443.8 and 412.1 nm lines. The average temperatures from the two ratios never deviated more than 4.4 eV. Each circle in figure 28 represents the average of the six measurements. The error bars extend one standard deviation above and below the point. The conditions for figure 28 were electrode voltage 8.0 to 15.5 kV, total anode-cathode current 0.6 to 1.2 A, pressure 8.4×10^{-5} to 1.85×10^{-4} torr, and magnetic flux density 1.07 to 3.52 T. Figure 28 shows that electron temperature tended to increase with the ratio of electrode voltage to pressure. The magnetic field did not have a strong influence on electron temperature.

One set of data was taken for the 504.7 and 471.3 nm lines for y from 0 to -4.38 cm. The intensities were sharply peaked at y = 0. The areas of each line profile were then Abel inverted. The ratio of intensities of the 504.7 and 471.3 nm lines was 0.501 for y = 0 and no Abel inversion and was 0.472 for the center of the plasma after an Abel inversion (part of the difference was due to the necessity to assume how the observed intensity varied beyond y = -4.38 cm). Hence there is no evidence that the Abel inversion has much effect on the center temperature except at the lowest temperatures where the temperature is very sensitive to the intensity ratio and the temperatures thus tend to be inaccurate anyhow.

VISUAL OBSERVATIONS

The maximum plasma input power and the length of individual runs were limited due to heating of the electrode assemblies. When operating the plasma at high input powers, the electrode assemblies were visually monitored via the mirrors shown in figure 3. This was done as a precaution against overheating and as a source of information about the plasma.

The plasma operated in either of two general modes. In the high current mode, local heating (to a red to white hot state) of the electrode assemblies occurred in a few seconds. The main regions of heating were the cathode tips, spots on the floating shields near the hole, and the lower corners of the floating shields that protect the vertically-mounted porcelain insulators as shown in figure 4. The water-cooled anodes did not visibly heat. In the low current mode the operating time could be extended to several minutes at voltages below 10 kV with only mild heating of the cathode tips. Operating in the low current mode at voltages above approximately 10 kV resulted in gradual heating of the electrode assemblies which in turn resulted in the plasma switching to the high current mode. In each mode, the rate of heating increased with current and voltage. Increasing the magnetic field strength accentuated the axial heating by constricting the plasma radially.

Though the parameters affecting the physical appearance of the plasma were interrelated, certain trends were noted. For both the hydrogen and helium plasmas, the plasma consisted of two distinct regions. One was an axial plasma column with a diameter at the midplane of about 2.5 cm enveloped by a second annular plasma with a mean diameter of approximately 20 cm. The shape of the axial plasma column conformed to the magnetic field lines with the maximum diameter located at the midplane and the minimum diameter at the mirror. However, the annular region often became azimuthally asymmetric resulting in a spiral-like plasma extension. When viewed in the mirror along the B-direction, the extension looked like a comma.

This spiral-like extension occurred at currents of about 0.2 A. Increasing the current from 0.2 to 0.6 A caused the spiral to constrict radially while extending azimuthally. At currents above 0.6 A the spiral extension smeared into a symmetric annular plasma becoming fainter with increasing current. However, the axial plasma column diameter increased with increasing current at currents greater than 0.6 A. In general, the diameter of annular plasma increased with voltage and decreased with magnetic field strength. Also occurring in the midplane in the high current mode was a vertical halo-shaped glow visible through a centerport window. The halo was approximately 1 cm wide and had a diameter greater than the 12.5 cm diameter port.

The hydrogen plasma (particularly the axial column) changed from a light blue color to a pink color upon switching from the low to high current mode. This indicates an increase in molecular dissociation at higher currents since the primary atomic hydrogen line is at 656.3 nm. This may be due to increased thermal dissociation of the feed gas as the cathodes heated up. The helium plasma remained purple in color for all operating conditions. However, when operating the helium plasma at 5 kV and 1.5 A there was a faint green glow around the periphery of the test section at midplane. The source of this glow was not established.

CONCLUDING REMARKS

The two major goals of the initial SUMMA experiments were successfully achieved. An electrode assembly for reliable steady-state operation was developed, and produced ion temperatures up to at least 5 keV in helium and at least 1.2 keV and 1.0 keV for H_2^+ and H^+ respectively in hydrogen. Ion temperatures were found to scale at least linearly as the ratio of power input-to-magnetic field strength. Water-cooled stainless steel anode rings were necessary to avoid local melting of the anodes.

To achieve higher ion temperatures at the higher magnetic fields, the electrodes must be designed to accommodate much higher thermal loads. Higher magnetic fields should produce higher ion densities.

The NPA data showed excellent signal-to-noise ratios, and were shown to agree well with a plasma model that was more complete than any model used previously for analyzing NPA results. The model included a randomized distribution superposed on an azimuthal drift, finite ion orbits, and radial variations in density and electric field strength.

The optical spectroscopy results for line broadening showed good qualitative agreement with the NPA results, but were about 50 percent higher. When a correction can be made for the strong magnetic field effects, it is believedthe optical results will be closer to the NPA results.

A very strong mass effect on ion heating was observed, with ion temperature increasing faster than linearly with mass as the mass went from H^+ to He^+ at constant electrode voltage and magnetic flux density.

The high ion temperatures and low electron temperatures, and the increase both in ion temperature and density with increased power, make this an attractive plasma heating method.

TABLE I

PARAMETERS FOR MAGNET SECTION IN

SIMPLE MIRROR CONFIGURATION

	cm
Bore diameter	41.3
Wide spacer width	19.7
Wide spacer access port diameter	13.6
Narrow spacer width	12.1
Narrow spacer access port diameter	7.6
Magnet module width	33.7

	Two inboard magnets powered
Maximum field at mirrors	5.2 T
Field at central plane	3.5 T
Mirror ratio	1.5
Distance between mirrors	77.5 cm

Table II Helium plasma discharge conditions for the curves of figure 8

Date	Run No.	Midplane Magnetic Field (T)	Electrode Voltage (kV)	Electrode Current (A)	Pressure (Torr)	Detector Signal at $\mathcal{E}_p$ (Rel. Units)	Most Probable Energy $\mathcal{E}_p$ (keV)	Half Width $\Delta\mathcal{E}$ (keV)	Ion Temp (eV)
3-29-74	6-1	2.66	4.0	0.62	1.54×10^{-4}	.12	1.40	-	-
"	6-2	2.66	4.8	1.34	1.54×10^{-4}	.45	1.92	1.74	390
"	6-3	2.69	7.2	0.88	1.23×10^{-4}	.55	3.20	2.80	480
"	6-4	2.71	8.9	0.85	1.15×10^{-4}	.73	3.80	3.74	620
"	6-5	2.72	10.8	1.03	1.09×10^{-4}	.76	5.20	4.78	680
"	6-6	2.74	14.0	0.84	1.01×10^{-4}	.87	7.14	8.26	1570
"	7-1	2.78	16.2	0.82	9.80×10^{-5}	.89	8.60	9.30	1600
"	7-2	2.81	17.5	0.85	9.20×10^{-5}	1.00	9.44	10.94	2200

Table III Helium plasma discharge conditions for the curves of figure 9

Date	Run No.	Magnetic Field (T)	Electrode Voltage (kV)	Electrode Current (A)	Pressure (Torr)	Detector Signal at $\mathcal{E}_p$ (Rel. Units)	Most Probable Energy $\mathcal{E}_p$ (keV)	Half Width $\Delta\mathcal{E}$ (keV)	Ion Temp (eV)	Electric Field (v/cm)
3-29-74	5-1	1.50	5.0	1.08	1.7×10^{-4}	1.00	4.4	3.3	350	2135
"	5-2	1.56	7.5	1.05	1.5×10^{-4}	1.03	5.4	5.0	650	1900
"	5-3	1.60	10.0	1.07	1.3×10^{-4}	.97	6.5	6.1	1000	1742
"	5-4	1.62	12.5	.87	1.2×10^{-4}	.62	7.6	8.2	2000	1372
"	5-5	1.65	17.7	.68	1.0×10^{-4}	.13	10.1	11.9	5000	1050

Table IV Hydrogen plasma discharge conditions for the curves of figure 10

Date	Run No.	Magnetic Field (T)	Electrode Voltage (kV)	Electrode Current (A)	Pressure (Torr)	Detector Signal at $\mathcal{E}_p$ (Rel. Units)	Most Probable Energy $\mathcal{E}_p$ (keV)	Half Width $\Delta\mathcal{E}$ (keV)	Ion Temp (eV)
4-1-74	12-1	1.37	16.6	.75	8.1×10^{-5}	.79	2.53	3.1	620
"	16-1	1.37	17.0	1.0	7.4×10^{-5}	.78	2.54	3.27	700
"	15-2	1.37	16.5	1.1	7.4×10^{-5}	.95	2.64	3.83	850
"	15-3	1.37	16.5	1.2	7.4×10^{-5}	1.00	3.15	4.35	950

Table V Hydrogen plasma discharge conditions for the curves of figure 12

Date	Run No.	Magnetic Field (T)	Electrode Voltage (kV)	Electrode Current (A)	Pressure (Torr)	Detector Signal at $\mathcal{E}_p$ (Rel. Units)	Most Probable Energy $\mathcal{E}_p$ (keV)	Half Width $\Delta\mathcal{E}$ (keV)	Ion Temp (eV)	Electric Field v/cm
4-2-74	5-1	1.07	5.0	1.0	1.0×10^{-4}	1.04	1.26	1.20	180	3000
"	5-2	1.07	6.0	1.0	1.0×10^{-4}	1.23	1.39	1.52	260	2500
"	5-3	1.07	8.0	1.0	1.0×10^{-4}	1.27	1.70	1.95	370	2500
"	5-4	1.07	10.0	1.0	1.0×10^{-4}	1.22	2.10	2.64	500	2000
"	5-5	1.07	12.0	1.0	1.0×10^{-4}	1.19	2.38	2.98	570	2300
"	6-1	1.07	14.0	1.0	1.0×10^{-4}	1.16	2.59	3.13	580	3000
"	6-2	1.07	16.0	1.0	9.7×10^{-5}	1.07	2.45	3.23	660	1900
"	6-3	1.07	17.7	1.0	9.6×10^{-5}	1.00	2.43	3.25	670	1800

Table VI Ion Temperature and Line Shift for Helium (From Line Profile Viewed Across Centerline of Plasma)

Midplane Magnetic Flux Density (T)	Electrode Voltage (kV)	Pressure (Torr)	Total Anode-Cathode Current (A)	Ion Temperature (eV)	Line Shift (nm)
3.52	8.0	1.15×10^{-4}	0.90	515	0.091
3.52	8.0	1.15	0.90	485	0.089
3.52	8.0	1.15	0.90	515	0.096
3.52	16.0	0.90	0.70	758	0.110
3.52	16.0	0.90	0.70	3670	0.366
2.72	8.0	1.18	0.96	846	0.133
2.72	8.0	1.18	0.96	610	0.125
2.72	15.5	0.95	0.90	2427	0.272
2.72	15.5	0.95	0.90	3442	0.391
1.84	16.0	0.92	0.75	7143	0.739
1.84	8.0	1.18	0.75	839	0.173
1.84	8.0	1.18	0.75	1664	0.291
1.84	8.0	1.18	0.75	4333	0.502
1.84	8.0	1.18	0.75	4128	0.436
1.07	8.0	1.79	0.92	6001	0.706
1.07	8.0	1.79	0.92	7055	0.768
1.07	15.5	1.57	1.20	6938	0.639
1.07	13.0	1.57	0.98	2693	0.531
1.07	13.0	1.57	0.98	3718	0.614
1.07	10.2	1.48	0.94	4274	0.643
3.52	15.8	0.92	0.65	177	0.054
3.52	13.0	0.92	0.65	949	0.137
3.52	13.0	0.92	0.65	1486	0.262
3.52	10.1	1.06	0.65	750	0.154
3.52	10.1	1.06	0.65	1066	0.183
3.52	8.0	1.18	0.60	507	0.112
3.52	8.0	1.18	0.60	478	0.102
3.52	6.0	1.40	1.08	449	0.060
3.52	6.0	1.40	1.08	412	0.056
3.52	5.0	1.40	0.58	324	0.058
3.52	5.0	1.40	0.58	250	0.054
3.52	8.0	1.40	0.80	559	0.100

Table VII Charge Exchange Neutral Temperature and Line Shift for Hydrogen (From Line Profile Viewed Across Centerline of Plasma)

Midplane Magnetic Flux Density (T)	Electrode Voltage (kV)	Pressure (Torr)	Total Anode-Cathode Current (A)	Charge-Exchange Neutral Temperature (eV)	Line Shift (nm)
1.07	15.9	9.0×10^{-5}	0.80	865	0.100
1.07	17.4	9.0×10^{-5}	0.90	1125	.029
1.07	8.0	9.0×10^{-5}	0.70	660	.044
1.84	16.0	5.8×10^{-5}	0.52	927	.077
1.84	9.5	5.9×10^{-5}	0.40	515	.054
2.72	16.4	5.2×10^{-5}	0.54	708	.052
2.72	10.0	4.5×10^{-5}	0.28	391	.098

REFERENCES

1. Reinmann, J. J. ; Swanson, M. C.; Nichols, C. R.; Obloy, S. J.; Nagy, L. A.; and Brady, F. J.: NASA Superconducting Magnetic Mirror Facility. NASA TM X-71480, 1973

2. Sigman, Donald R.; and Reinmann, John J.: Steady-State Hot-Ion Plasma Produced by Crossed Electric and Magnetic Fields. NASA TM X-2783, 1973.

3. Sigman, Donald R.; Reinmann, John J.; and Lauver, Milton R.: Bull. Am. Phys. Soc., Series II, vol. 18, no. 10. Oct. 1973, p. 1296.

4. Sigman, Donald R.; Reinmann, John J.; and Lauver, Milton R.: Parametric Study of Ion Heating in a Burnout-Type Device (HIP-1). NASA TM X-3033, 1974.

5. Anon.: Thermonuclear Division Annual Progress Report for Period Ending December 31, 1970. Rep. ORNL-4688, Oak Ridge National Lab., Aug. 1971, pp. 77-89.

6. Hirose, A.; and Alexeff, I.: Electrostatic Instabilities Driven by Currents Perpendicular to an External Magnetic Field. Nuclear Fusion, vol. 12, no. 3, May 1972, pp. 315-323.

7. Englert, G. W.; Reinmann, J. J.; and Lauver, M. R.: Guiding Center Model to Interpret Neutral Particle Analyzer Results. Presented at the First IEEE International Conf. on Plasma Science (IEEE Nuclear and Plasma Sciences Society, sponsor), Univ. of Tenn., Knoxville, Tenn., May 15-17, 1974. NASA TM X-71555.

8. Lucas, E. J.: Stekly, Z. J. J.; deWinter, T. A.; Laurence, J. C.; and Coles, W. D.: Advances in Cryogenic Engineering, vol. 15, Plenum Press, New York, 1970, pp. 167-177.

9. Laurence, J. C.; Coles, W. D.; Brown, G. V.; and Meyn, E. H.: ibid., pp. 178-183.

10. Valckx, F. P. G.: Electrostatic Analyzer for the Detection of Fast Neutral Particles. NASA TT F-11458, 1968.

11. Kieffer, L. J.; and Dunn, G. H.: Dissociative Ionization of H_2 and D_2. Physical Review, vol. 158, no. 1, June 5, 1967

12. Stirling, W. L.: Lifetime of Hot-Ion Plasma in a Mirror Machine. Phys. Fl., vol. 15, no. 4, April 1972, pp. 688-692.

13. Alexeff, I.; Guest, G. E.; McNally, J. R. Jr.; Neidigh, R. V.; and Scott, F. R.: Doppler-Broadened Spectral Emission from the Turbulently Heated Plasma of Burnout V. Phys. Rev. Ltrs., vol. 23, no. 6, Aug. 11, 1969, pp. 281-283.

14. Sutton, George W.; and Sherman, Arthur: Engineering Magnetohydrodynamics. McGraw-Hill Book Co., Inc., 1965, p. 72.

15. Sato, T.; deKock, L. C. J. M.; and Winkel, Th. G. A.: Ion Temperature Measurements in the Range of 0.1-1 eV by Means of the Doppler Broadening of the 4686 Å He II Line. Plasma Phys., vol. 15, no. 9, Sept. 1973, pp. 921-925.

16. White, Harvey Elliott: Introduction to Atomic Spectra. McGraw-Hill Book Co., Inc., 1934, pp. 168-169.

17. Sovie, Ronald J.: Spectroscopic Determination of Electron Temperature and Percentage Ionization in a Helium Plasma. Phys. Fl., vol. 7, no. 4, Apr. 1964, pp. 613-614.

18. Sovie, R. J.: The Effects of Cascading and Metastable Atoms on the Determination of Electron Temperature from Relative Line Intensities in a Tenuous Helium Plasma. J. Quant. Spectrosc. Radiat. Transfer, vol. 8, no. 3, Mar. 1968, pp. 833-838.

19. Latimer, I. D.; Mills, J. I.; and Day, R. A.: Refinements in the Helium Line Ratio Technique for Electron Temperature Measurement and Its Application to the Precursor. J. Quant. Spectrosc. Radiat. Transfer, vol. 10, no. 6, June 1970, pp. 629-635.

20. DeVos, J. C.: A New Determination of the Emissivity of Tungsten Ribbon. Physica, vol. 20, no. 7, July 1954, pp. 690-714.

APPENDIX A

Details of the NPA Detector and Electronics System

The detectors used were Bendix Channeltron electron multipliers similar to model CEM-4039 but with a 3.2 mm cylindrical extension on the front of the cone to give a more uniform response across the entrance aperture. A photograph of the detector assembly is shown in figure A1. A schematic wiring diagram of the detector and the current-to-voltage converter are shown in figure A2. The detector delivers output current at high impedance into a current-to-voltage converter or current amplifier which also serves as a coaxial line driver. Up to 100 mA can be delivered into 100 ohms at 10 MHz by the Burr-Brown Model 3342/15C, wideband, fast settling, inverting operational amplifier with FET input. A three-position switch selects gain of 10^6, 10^7, or 10^8 V/A. Inverse parallel-connected diodes protect the amplifier from plasma induced transients. The amplifier, which is housed in a dual chassis enclosure to minimize 60 Hz pickup, is connected directly to the Channeltron output to reduce the effects of lead inductance and capacity.

To obtain rapid sweeps of the energy spectrum for a given ion species an electronic feedback circuit was developed. The electronics system provides excitation voltage to the electrostatic deflection plates in response to a ramping magnetic field in the bending magnet. This is done automatically in accordance with the theoretical expression,

$$V = \frac{kB^2}{M}$$

where k is a constant determined from the NPA deflection system geometry; B is the magnetic field in the bending magnet gap; and M is the mass-to-charge ratio of the species selected for examination. The required relationship for B vs V may differ slightly from the theoretical expression given above because of fringing magnetic fields and the influence of the SUMMA magnetic field.

A block diagram of the electronics system is shown in figure A3. Magnetic flux density in the gap is measured with an error less than $\pm$ 0.4% full scale by a solid-state gaussmeter (Bell Model 620) using a high performance transverse Hall probe. The auxiliary output of the gaussmeter, adjusted to give 5.00 V dc full scale output, is applied as input to the electronics box. The gaussmeter output may be bypassed by the automatic-manual switch for powering the electrostatic deflection plates independent of the bending magnet and to facilitate overall system calibration.

The electronics box contains solid-state analog multiplier/dividers of the variable transconductance type which perform the mathematical operations of squaring (B^2) and division ($1/M$), a summing network, and an output amplifier. Also contained but not shown in figure 9 are externally adjustable voltages for calibration, testing, and trouble-shooting. Both the multiplier/dividers and the output amplifier are capable of slewing rates in excess of 6 V/μsec.

The M Adjust input to the divider is a high resolution potentiometer circuit which is set to a voltage corresponding to the mass-to-charge ratio of interest. As indicated in figure 9, this voltage, e_3, also depends upon the full scale range selector position of the gaussmeter. The range selector is set to 0.3 T full scale for lower mass numbers because this raises the divisor voltage, thereby increasing the accuracy of the divider.

The output amplifier is a transistor-input differential operational amplifier connected in a low-gain (0.7 to 1.7) inverting configuration. A summing network fed by a potentiometer offset control and a solid-state tunable oscillator provides for superposing an ac signal on the dc output level. The offset control corrects for initial offset as well as long term drift of the output amplifier, while the oscillator corrects for errors between the required curve of B vs V for a given M number and the theoretical curve which is actually generated by the electronics system. Superposition of the oscillator output on the theoretical curve results in a curve which crosses many times through the required curve. At each crossing, the peak detector current is the desired result. However, the oscillator is seldom needed because the actual output is an excellent fit to the required curve. Adjustment of the oscillator in frequency from 0.9 Hz to 27 Hz and in amplitude from 0 to 200 mV peak-to-peak results in a wide potential for curve correction as well as in the number of curve crossings.

The positive output of the electronics box feeds the voltage programming input of a dual power supply system. The electrostatic deflection plates and a high impedance instrumentation circuit (1000:1 divider) which is balanced-to-ground are driven by this system. The system operates from a single voltage programming source, does not require dc isolation from the gaussmeter or electronics box which are grounded, and provides a symmetrical output, both positive and negative with respect to ground. One leg of the power supply system includes a programming interface unit (Kepco NTC-2000). This is an inverting operational amplifier, which raises the positive programming signal to the desired voltage level and then feeds the noninverting feedback terminals of Power Supply 1, making its output positive with respect to ground. Power Supply 2 which is directly programmed at its inverting input has a negative output with respect to ground. Identical power supplies (Kepco OPS-2000) are used to give symmetrical static and dynamic characteristics referenced to ground. Each supply can deliver an output

of 0-2000 V dc and 0-10 mA at a slewing rate in excess of 1 V/μsec. The programming amplifiers of each power supply are set by external potentiometers for a gain ranging from 200 to 400.

SUMMA FACILITY

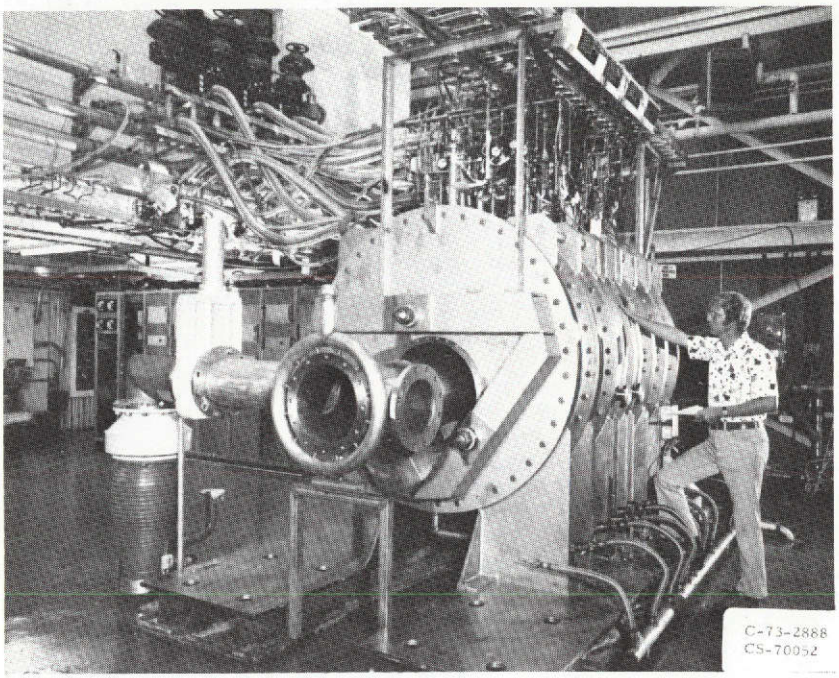

Figure 1

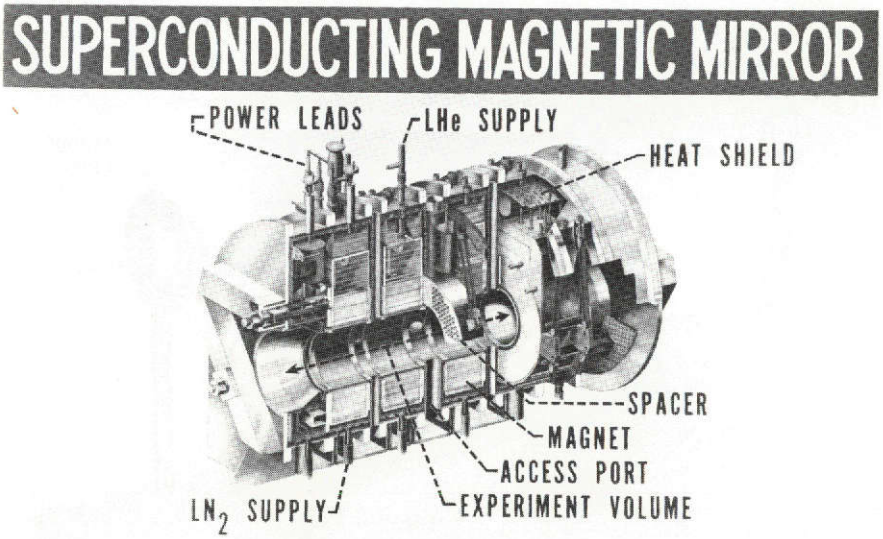

Figure 2. - Cutaway view of SUMMA.

TEST SECTION AND MAGNETIC FIELD CONFIGURATION

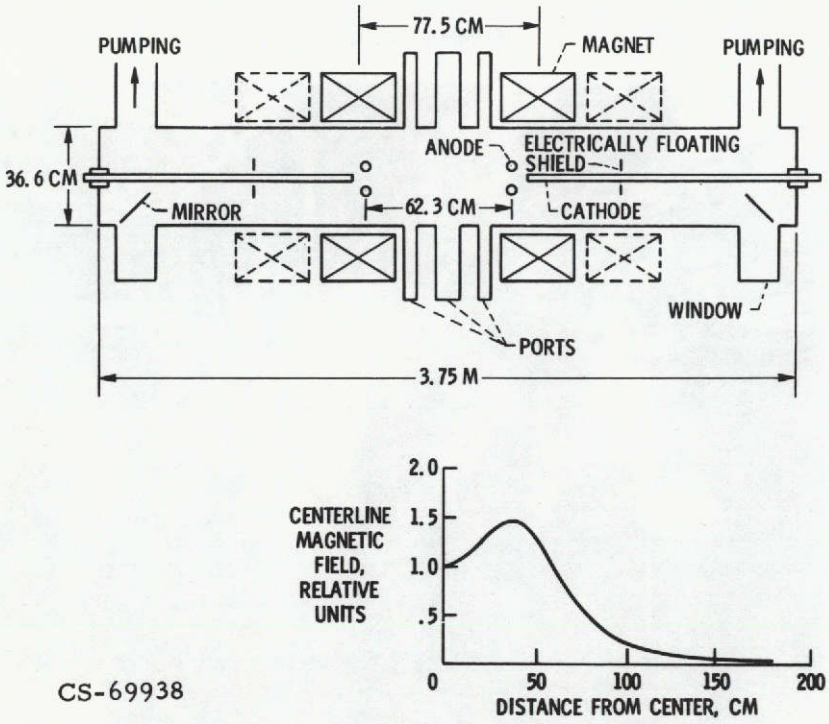

Figure 3

SUMMA ELECTRODE ASSEMBLY

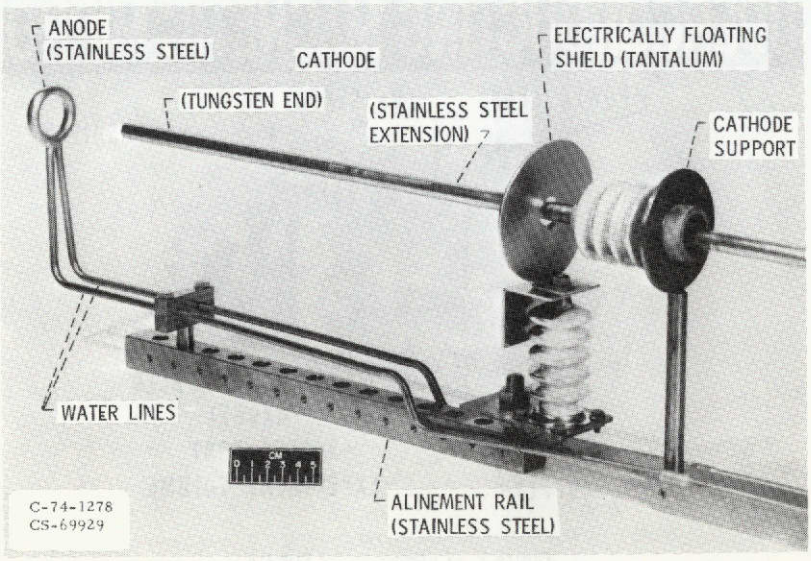

Figure 4

CATHODE CROSS-SECTION

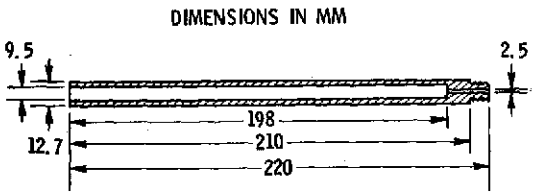

Figure 5 CS-70053

CHANGE EXCHANGE NEUTRAL PARTICLE ANALYZER

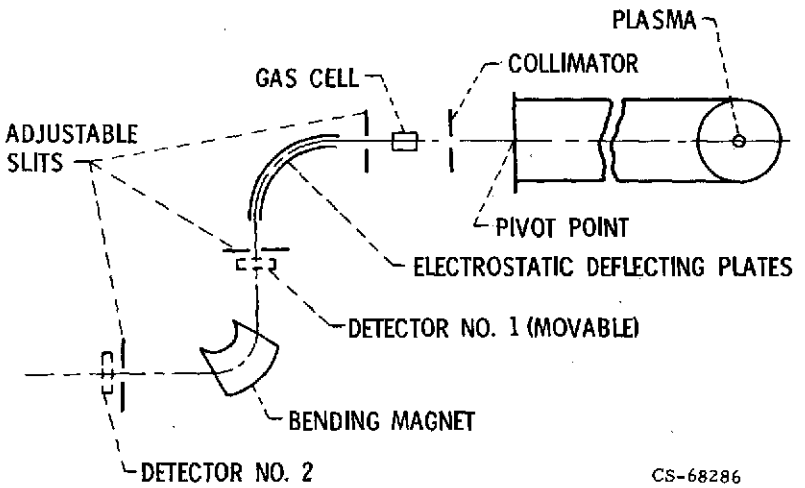

Figure 6

EMISSION OPTICAL SPECTROSCOPY APPARATUS

NOT TO SCALE

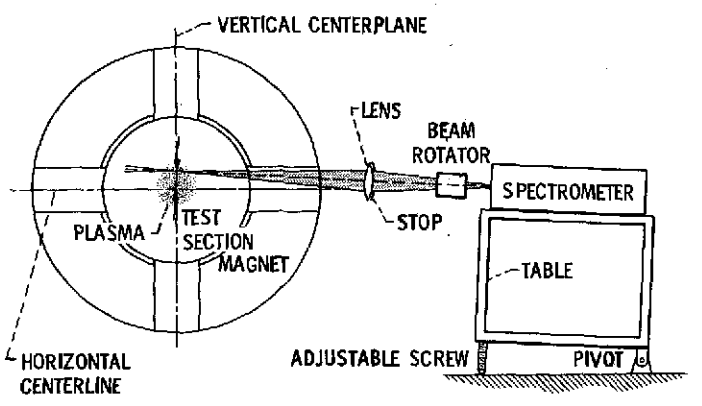

Figure 7

E-7984

He^+ ENERGY DISTRIBUTIONS FOR EIGHT ELECTRODE VOLTAGES

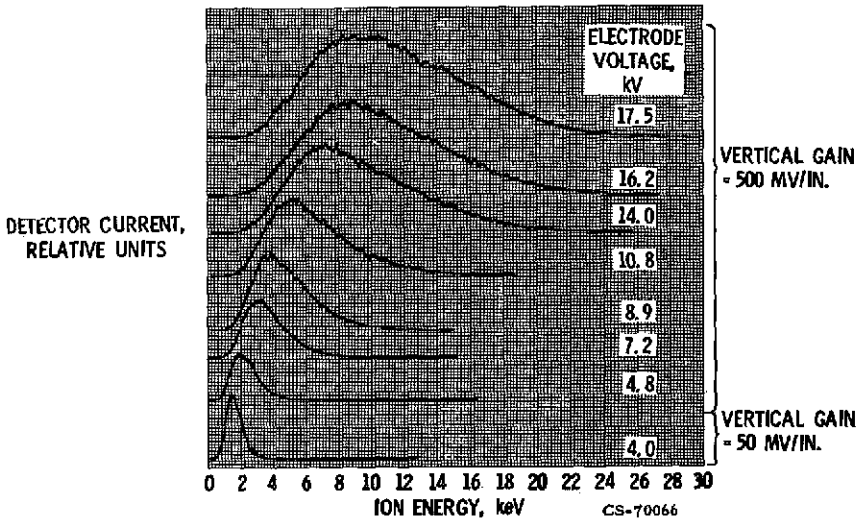

Figure 8

COMPARISON OF UNIFORM E THEORY WITH NPA DATA FOR He

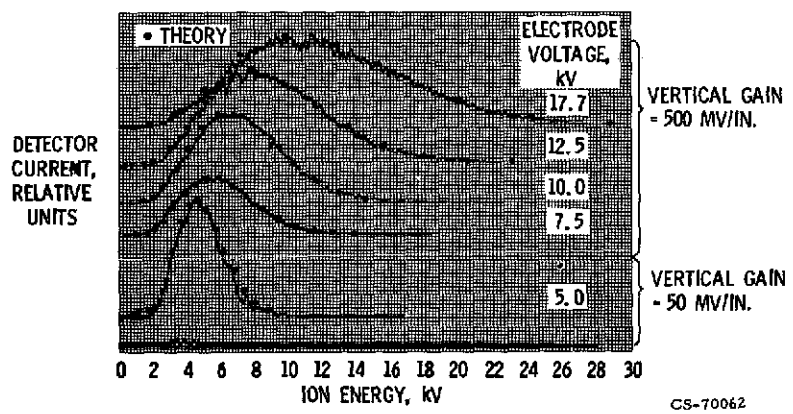

Figure 9

H⁺ENERGY DISTRIBUTIONS FOR FOUR ELECTRODE CURRENTS

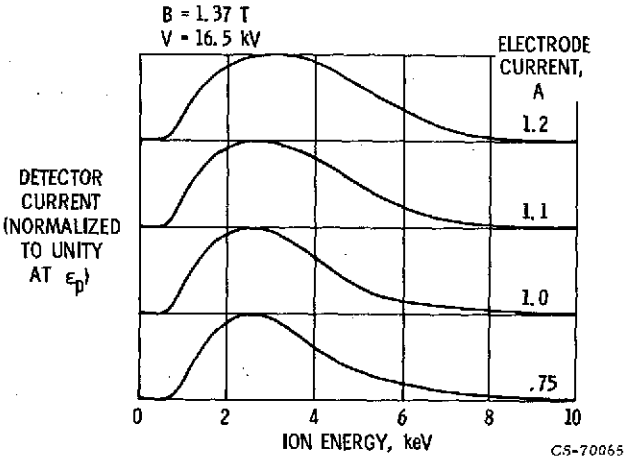

Figure 10

E-7984

RELATIVE DETECTOR CURRENTS OF H^+, H_2^+ AND C^+ FOR HYDROGEN

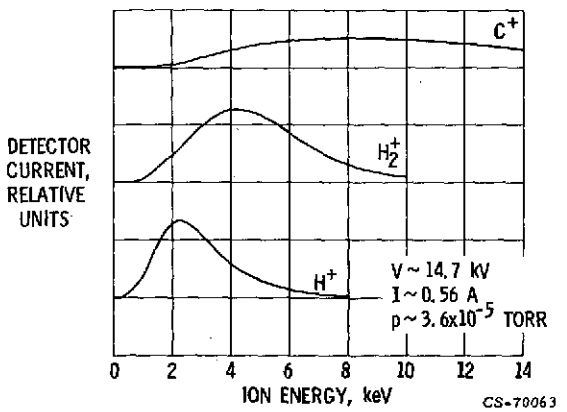

Figure 11

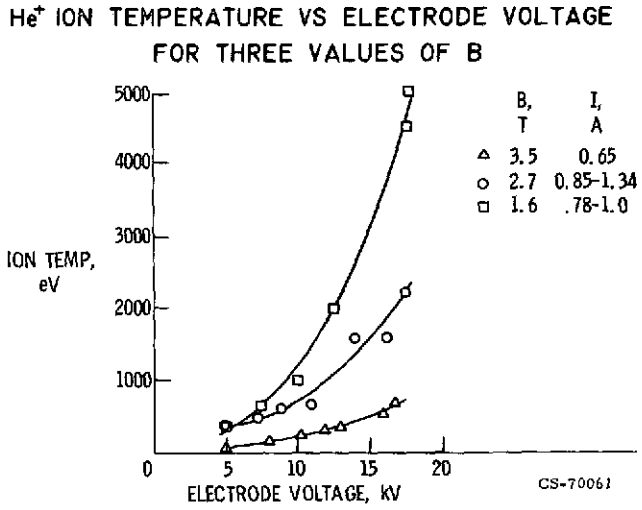

Figure 12

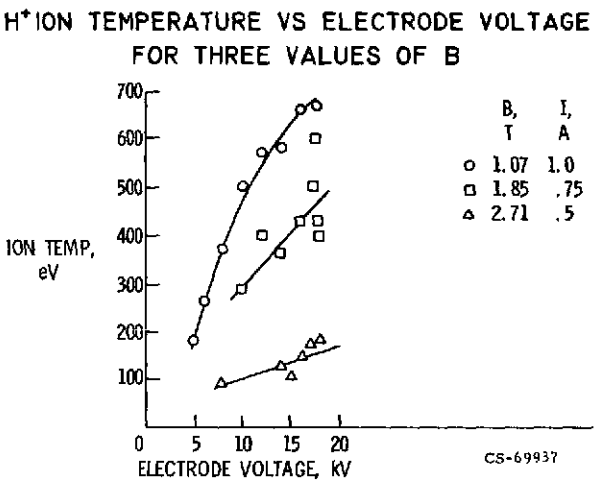

Figure 13

H_2^+ ION TEMPERATURE VS ELECTRODE VOLTAGE FOR TWO VALUES OF B

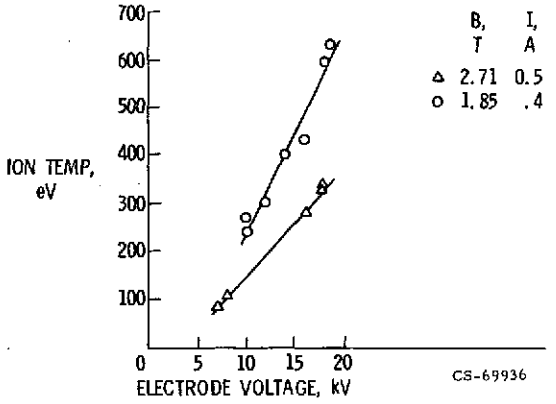

Figure 14

He^+ ION TEMPERATURE VS P/B FROM NPA

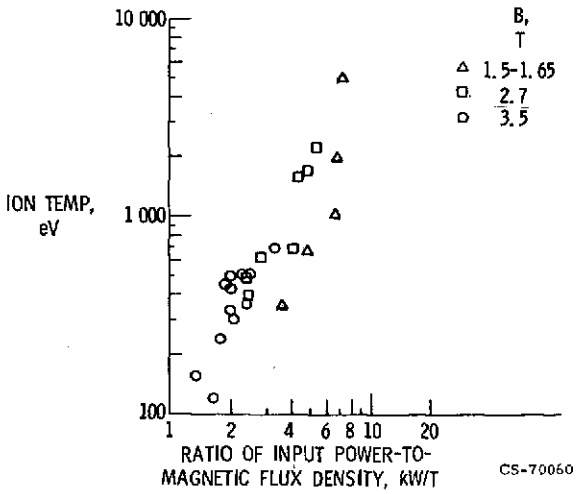

Figure 15

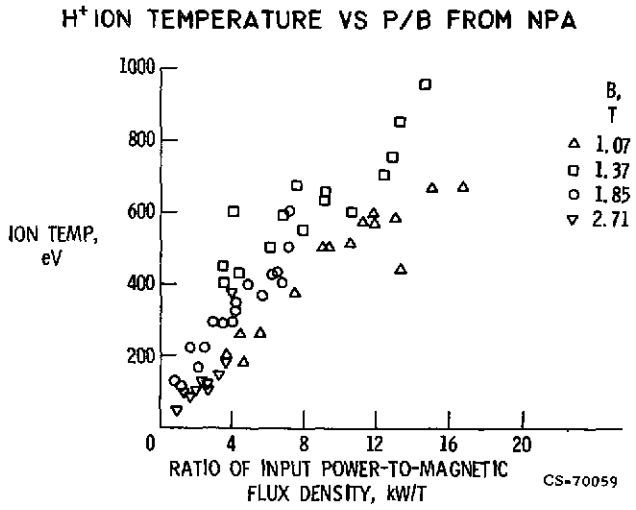

Figure 16

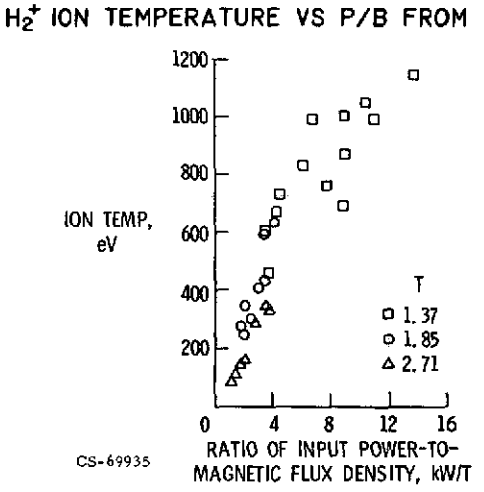

Figure 17

ION ENERGY SPECTRUMS FOR THREE DIFFERENT SPECIES

	ELECTRODE		MAGNET
	VOLTAGE, kV	CURRENT, A	FIELD, T
He	12.5	0.87	1.6
H^+, H_2^+	11.8	.77	1.37

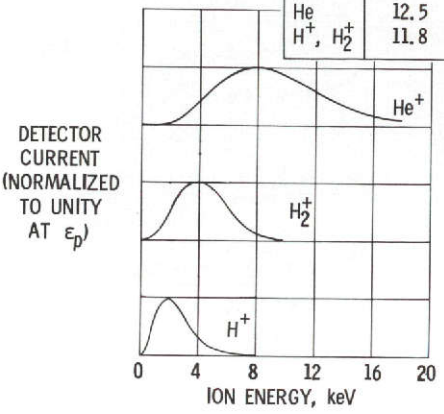

Figure 18

He^+ 468.6 NM—NORMAL LINE PROFILE

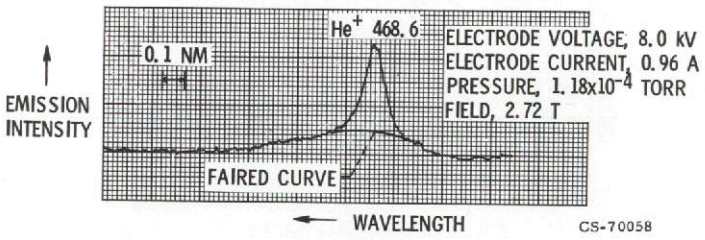

Figure 19

He^+ 468.6 NM ANOMALOUS LINE PROFILE

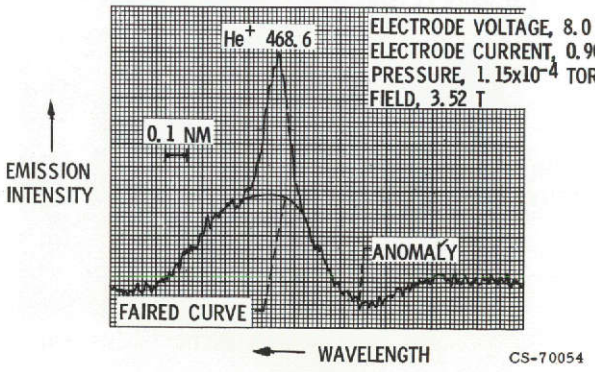

Figure 20

He^+ 468.6 NM LINE SHOWING WIDE COMPONENT SHIFT WITH CHORD POSITION

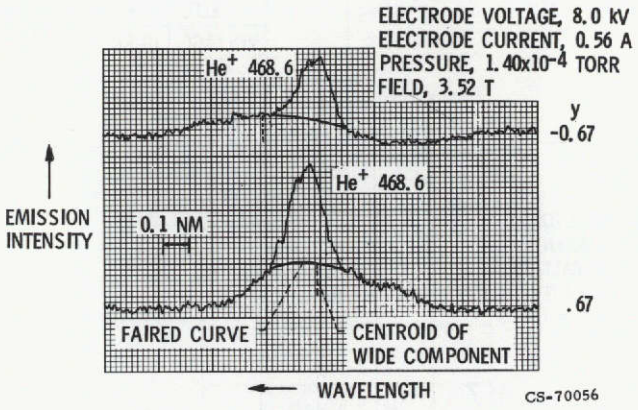

Figure 21

$H\beta$ LINE WITH MINIMUM H_2 INTERFERENCE

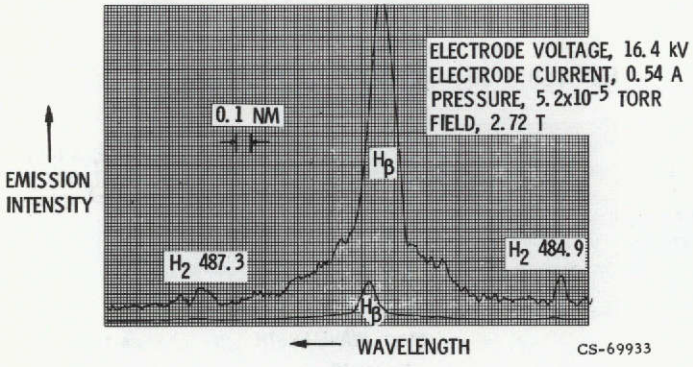

Figure 22

$H\beta$ LINE WITH MAXIMUM H_2 INTERFERENCE

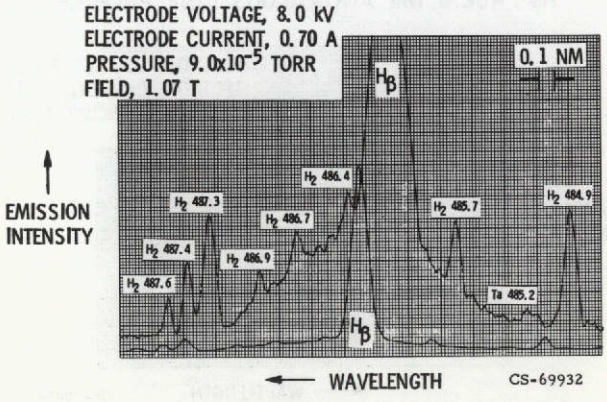

Figure 23

E-7984

He^+ ION TEMPERATURE VS P/B FROM LINE PROFILES

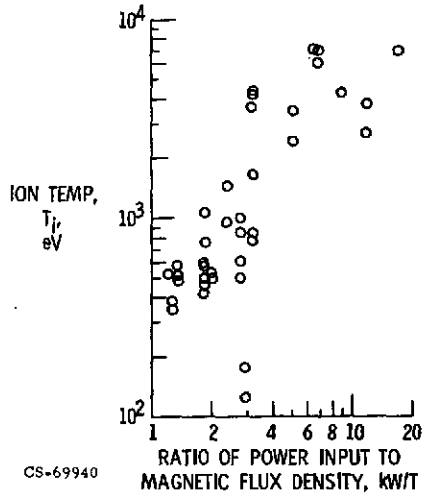

Figure 24

H^+ ION TEMPERATURE VS P/B FROM LINE PROFILES

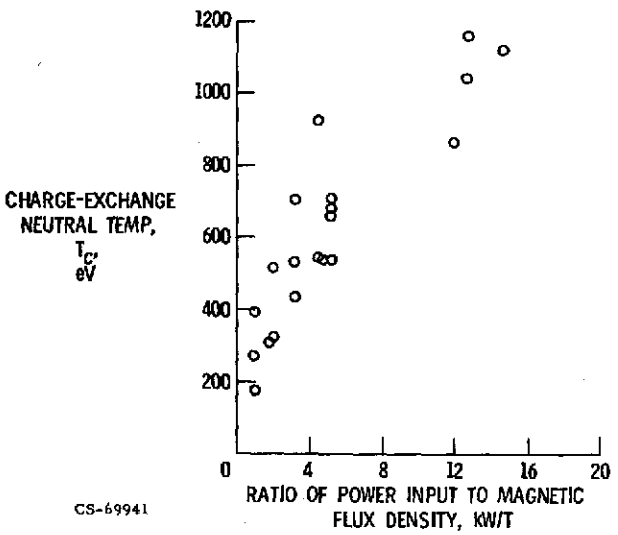

Figure 25

SHIFT OF WIDE CONTRIBUTION VS CHORD POSITION FOR He

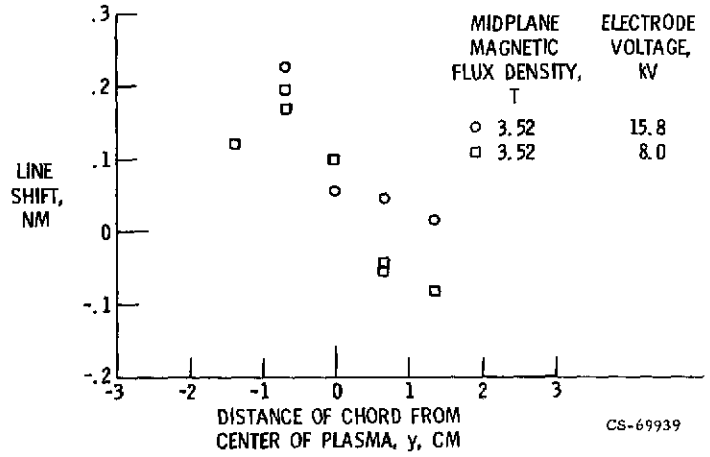

Figure 26

SHIFT OF WIDE CONTRIBUTION VS CHORD POSITION FOR H

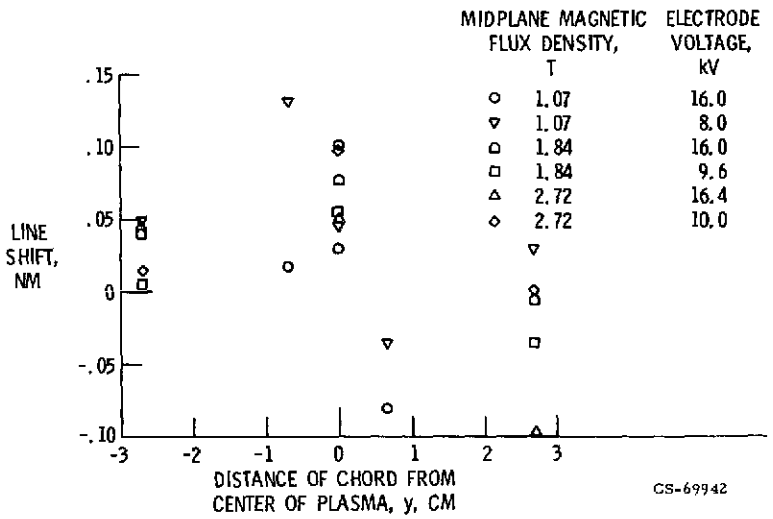

Figure 27

ELECTRON TEMPERATURE VS RATIO OF ELECTRODE VOLTAGE TO BACKGROUND PRESSURE FOR He

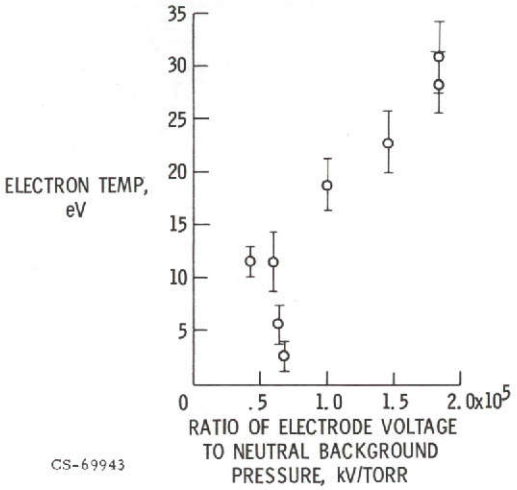

Figure 28

PARTICLE DETECTOR ASSEMBLY

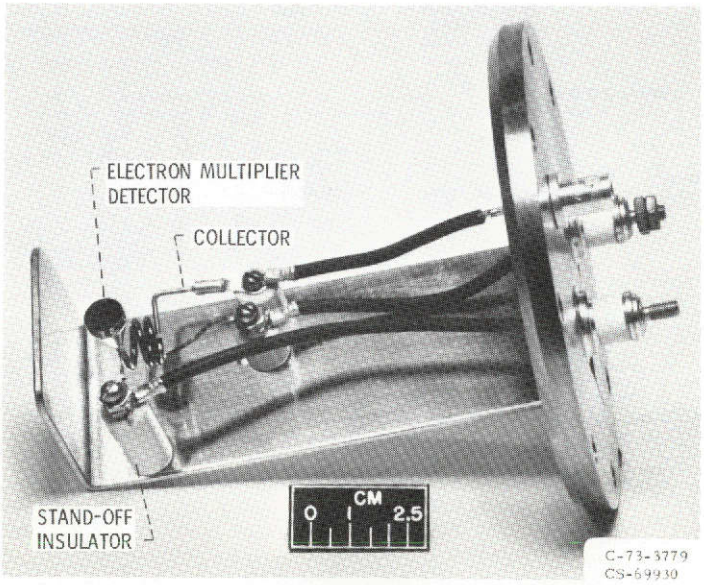

Figure A1

DETECTOR AND CURRENT-TO-VOLTAGE CONVERTER

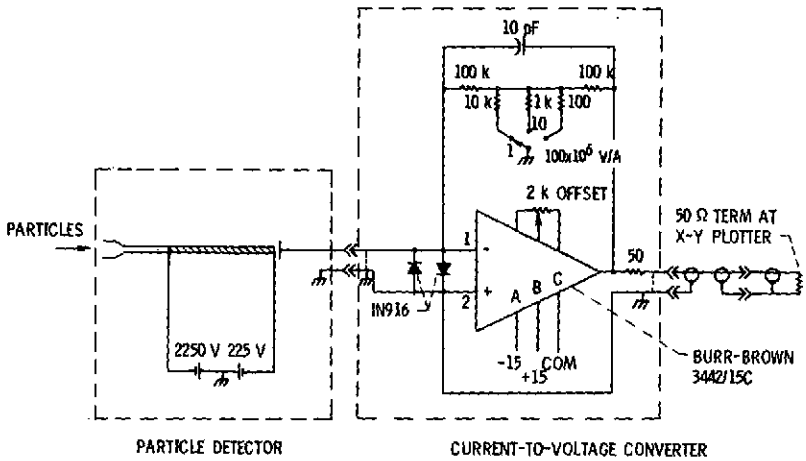

Figure A2

CS-70057

BLOCK DIAGRAM OF ELECTRONICS FOR NPA

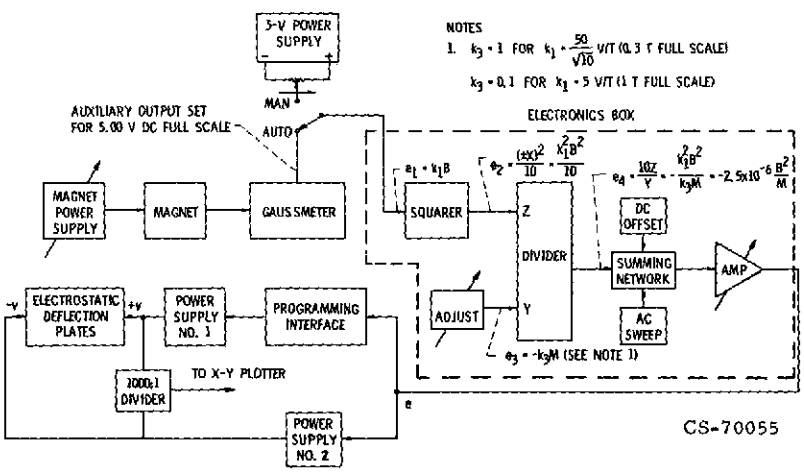

CS-70055

Figure A3

NASA-Lewis